Hollow Core Inhibited Coupled Antiresonant Terahertz Fiber: A Numerical and Experimental Study

Jakeya Sultana [ID], Md. Saiful Islam [ID], *Member, IEEE*, Cristiano M. B. Cordeiro [ID],
Md. Selim Habib [ID], *Senior Member, IEEE*, Alex Dinovitser [ID], *Graduate Student Member, IEEE*, Mayank Kaushik,
Brian W.-H. Ng [ID], *Member, IEEE*, Heike Ebendorff-Heidepriem [ID], and Derek Abbott [ID], *Fellow, IEEE*

Abstract—In this article, a hollow core antiresonant photonic crystal fiber is analyzed for terahertz applications. A numerical analysis of the proposed fiber is first carried out to minimize coupling between the core and cladding modes. The modeling of the scaled-up and inhibited coupling fiber is carried out by means of a finite element method, which is then demonstrated using a Zeonex filament fiber, fabricated by fused deposition modeling of 3-D printing technology. The simulation is carried out to analyze both the transmission and possibility of refractometric sensing, whereas the experimental analysis is carried out using terahertz time-domain spectroscopy, and supports our numerical findings, illustrating how the proposed fibers can be used for low-loss transmission of terahertz waves. The simplicity of the proposed fiber structures facilitates fabrication for a number of different transmission and sensing applications in the terahertz range.

Index Terms—3-D printing, antiresonant fiber, optical fiber, THz-TDS, terahertz.

I. INTRODUCTION

THE TERAHERTZ region in the electromagnetic spectrum located between the microwaves and the infrared regions opens a new frontier generating new technical applications and fundamental research problems. The interest in terahertz technology is increasing because of its potential application in sensing, especially for label-free and noninvasive molecular detection, detection of DNA hybridization, security scanning, pharmaceutical drug testing, and high-speed short-range optical communications [1]–[3]. Terahertz also has potential in spectroscopy for biomedical applications, because it has stronger interaction with polar molecules than radiation in, say, the microwave region [4]–[7]. Despite the potential of the terahertz band, it is still in the development phase as many terahertz systems are bulky and depend on free space for transmission. The free space transmission of terahertz radiation experiences significant undesirable absorption losses due to the coupling with atmospheric components that reduce transmission efficiency.

As a primary solution for low-loss terahertz transmission, prior studies have proposed several polymer-based fibers, including subwavelength fibers [8], porous core fibers [11], and hollow core fibers [12]–[14]. The guided mode field in subwavelength fibers extends far into the surrounding air to minimize the overlap of the propagation mode and the lossy fiber material, and has high power fraction outside the core. Further reduction of propagation loss can be achieved by inserting a porous structure into the core. However, they are very sensitive to external perturbations and bending [15], which is very challenging in many applications.

Hollow core fibers consist of an air-core surrounded by a structured cladding, which confine most of the power within the air-core region. As a result, the influence of material loss is minimized. Hollow core fibers have attracted significant attention because of their novel characteristics. For example, hollow core fibers have utility in the sensing of gas/liquid samples [16], where strong electromagnetic interaction in the core enhances the sensing performance. In transmission, the ultra-low nonlinearity reduces the signal noise [17]–[19]. In high-power pulse delivery [20], light guidance in air avoids the damage threshold of core material. Several designs based on the cladding structure in hollow core fiber have been proposed, such as photonic

Jakeya Sultana, Alex Dinovitser, Brian W.-H. Ng, and Derek Abbott are with the School of Electrical & Electronic Engineering, University of Adelaide, Adelaide, SA 5005, Australia (e-mail: jakeya.sultana@adelaide.edu.au; alex.dinovitser@adelaide.edu.au; brian.ng@adelaide.edu.au; derek.abbott@adelaide.edu.au).

Md. Saiful Islam is with the School of Electrical & Electronic Engineering, University of Adelaide, Adelaide, SA 5005, Australia, and also with the Institute for Photonics & Advanced Sensing (IPAS), University of Adelaide, Adelaide, SA 5005, Australia (e-mail: mdsaiful.islam@adelaide.edu.au).

Cristiano M. B. Cordeiro is with the Institute of Physics, University of Campinas, Campinas 13083-859, Brazil, and also with the Institute for Photonics & Advanced Sensing (IPAS), University of Adelaide, Adelaide, SA 5005, Australia (e-mail: cmbc@ifi.unicamp.br).

Md. Selim Habib is with the Department of Electrical and Computer Engineering, Florida Polytechnic University, Lakeland, FL 33805-8531 USA (e-mail: mhabib@floridapoly.edu).

Mayank Kaushik is with the Defence Science & Technology (DST) Group, Edinburgh, SA 5111, Australia (e-mail: Mayank.Kaushik@dst.defence.gov.au).

Heike Ebendorff-Heidepriem is with the Institute for Photonics & Advanced Sensing (IPAS), University of Adelaide, Adelaide, SA 5005, Australia (e-mail: heike.ebendorff@adelaide.edu.au).

Color versions of one or more of the figures in this article are available online at https://ieeexplore.ieee.org.

Digital Object Identifier 10.1109/TTHZ.2020.3031727

band-gap (PBG) [12], [13] and Kagome-type fibers (inhibited guiding fibers/antiresonant reflection fibers) [14], [21].

For PBG, the propagation mode field is confined within the core with the help of band-gap reflectors, which prohibits the field from extending into the periodic structures over specific frequencies. In these fibers, coupling of the core mode to the cladding mode is forbidden, thus confining light with low loss. The most common PBG-type fibers tend to have spectrally narrow transmission windows and suffer from surface scattering loss. Moreover, high air filling fraction as well as a strictly periodic cladding structure is needed to obtain an efficient and broad band-gap [12], [13], which all increase the fabrication complexity.

Unlike the PBG-type fibers that guide light by means of a photonic band-gap in the cladding, guiding of light in Kagome-type fibers [22] is based on the low density of cladding modes and small spatial overlap of cladding modes with core modes [23]–[25]. Inhibited coupling usually shows abrupt transmission dips at the edge of the transmission band caused by the weak finite coupling between core and cladding modes. Recently, these type of fibers have sparked great interest owing to their transmission properties, such as broad bandwidth, low power overlap with the absorbing material region, low dispersion, and low-loss levels. The terahertz air-core microstructured fiber was the first experimental demonstration of Kagome-type fiber with an attenuation loss of $0.02 \, \text{cm}^{-1}$ [26], which was constituted from a periodic cladding structure of Teflon tubes with a core diameter of 5.5 mm. It was proven that the optical properties of the antiresonant fiber largely depend on the first air-cladding layer surrounding the air-core [27]. Subsequently, in order to control the modal content and attenuation, several types of simplified antiresonant fibers with one air-cladding layer have been proposed, investigated, and fabricated, including hollow core antiresonant photonic crystal fiber (HC-ARPCF) with a circular antiresonant tube [27], [28] half-elliptical antiresonant elements [30], [31], ice cream-cone shaped antiresonant tubes [32], and nested and adjacent nested tubes [29], among others.

The simplified structure features a nodeless core boundary, a negative core curvature, and a single-tube cladding layer [34], often called tube lattice fiber. Nodeless core boundary means that the tube elements do not touch. The negative core curvature is found to enhance the inhibited coupling between the core and cladding modes [32], while the nodeless core boundary helps to reduce the loss caused by Fano-resonance [37]. Recently, nodeless single-layer negative curvature HC-ARPCF was proposed and experimentally demonstrated for terahertz wave guidance [34]. Compared to all the previously reported HC-PBG fibers, the HC-ARPCF is relatively simple. Using commercially available polymethyl-methacrylate (PMMA), it was experimentally confirmed that terahertz waves can be successfully guided through the central core with excellent mode characteristics and controllable bandwidth. Moreover, the capillary tubes provide resonant coupling to core higher order modes (HOMs) to provide HOM suppression [38]. The difference of propagation loss between the fundamental and the higher order core modes can be increased by a proper choice of cladding features, thus allowing microstructured fibers to be effectively single mode [38]. In

2015, Lu *et al.* [35] reported a Zeonex-based fiber with the lowest loss of 1 dB/m at low terahertz for the core diameter and the tube thickness are of 3.84 and 0.378 mm, respectively. In 2018, Nazarov *et al.* [36] demonstrated the possibility of manufacturing a single-mode flexible waveguide, with a loss of 7 dB/m within 1.9–2.2 THz for 1.3-mm core diameter. However, the antiresonant fibers of [34]–[36] are fabricated by capillary stacking and stack and drilling techniques, where a large-scale fiber-drawing tower for the drawing process greatly increases fabrication cost. The structured preform with scaled-up dimensions, produced by capillary stacking and stack and drilling techniques, requires drawing to obtain the microstructure.

The first development of the HC-ARPCF was introduced for visible to mid-infrared, with surprisingly low propagation loss [39], but also with considerable bending loss [40]. Although these types of optical fibers have been developed for high-power beam delivery [40] for the medical [41] and industrial [42] work, there has been limited work done on anitresonant terahertz transmission and sensing. Therefore, there is scope for developing antiresonant fiber for low-loss terahertz transmission and sensing, for important applications including analyte identification and concentration monitoring, chemical and environmental pollution monitoring, medical breath analysis, leaky molecule detection for various toxic, volatile or explosive gases, etc.

To address the above requirements, we report our initial work with a Zeonex-based nodeless single-layer negative curvature HC-ARPCF. The aim is to introduce inhibited coupling between core and cladding mode for low-loss terahertz guidance, and resonant coupling between HOM and cladding modes for single-mode guidance, through the parametric optimization of core and cladding inner diameter. These optimized fiber can then efficiently transmit terahertz waves with low propagation loss and improved core power fraction, applicable for transmission and sensing in the terahertz regime. We organize the work as follows. In Section II, we discuss the fiber geometry, design, and 3-D fabrication process; Section III introduces the mechanism of inhibited coupling and demonstrates the numerical characterization of different optical properties required for transmission and sensing, while Section V highlights the experimental analysis using terahertz time-domain spectroscopy (THz-TDS).

II. FIBER GEOMETRY: DESIGN AND FABRICATION

A. Fiber Geometry and Design Methodology

Fig. 1 shows the schematic of the proposed HC-ARPCF. Cyclo-olefin polymer, commercially known as *Zeonex* [43] and [44], has been used as a background material due to its unique characteristics compared to polytetrafluoroethylene, polyethylene, PMMA, Teflon, etc. [45], [76]. These include i) low bulk material absorption loss of $0.02 \, \text{cm}^{-1}$, ii) low dispersion, constant refractive index of 1.5352 in 0.1 to 4.5 THz frequency range, iii) high glass transition temperature, and iv) insensitivity to humidity [46].

To perform the numerical simulations, we use a finite-element based "Eigenvalue solver" (COMSOL Multiphysics). For the wave equation, the perfectly matched layers are notional absorbing layers, outside the fiber domain, that assist in solving
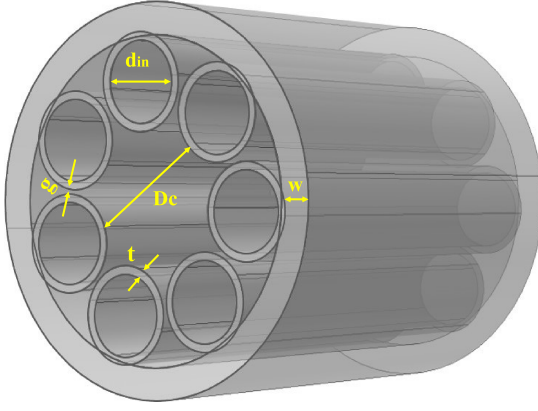
Fig. 1. Cross section of the seven-tube inhibited coupled HC-ARPCF fiber. The material used is Zeonex. The fiber geometry has been set with core diameter $Dc = 3$ mm, strut thickness of polymer tube $t = 0.09$ mm, inner capillary diameter $din = 2.04$ mm, fiber outer diameter OD = 8.38 mm, and seven-antiresonant tube.

the open boundary problems during simulation. This is not just one line, but rather a number of elements or 15 in our case. The simulation window is circular. In order to achieve improved accuracy in simulation, great care is taken in the use of an extremely fine mesh size. We use a nonuniform mesh. We maintain a smaller mesh size in the antiresonant tubes compared to the air region [51]–[53]. The mesh size in the antiresonant tubes is chosen at $\sim\lambda/10$, and in the air-region $\sim\lambda/5$, which is an extremely fine mesh size for obtaining accurate results.

The initially optimized seven-tube antiresonant fiber (ARF) geometry is set with a core diameter $Dc = 3$ mm, tube strut thickness $t = 0.09$ mm, inner capillary diameter $d_{\text{in}} = 2.04$ mm, and fiber outer diameter OD = 8.38 mm, where g is the gap between two adjacent antiresonant tubes. Note that we selected seven capillary tubes as the cladding because it was previously shown that seven- or eight-tube elements exhibit the optimal HOM suppression, required for single-mode operation [47]. Also note that, in order to choose the optimum dimension of the proposed fiber, extensive numerical analyses were carried out and the performances were observed by varying the fiber core diameter, strut thickness, gap between antiresonant tubes, and outer diameter.

The light guidance of the proposed fiber occurs on the basis of the antiresonant reflecting optical waveguide (ARROW) model [30], [48] and inhibited (reduced) coupling [23], [24] between core and cladding modes. The thin struts around the core support antiresonance and inhibited coupling between core and cladding modes, and enhance the guidance as it introduces a phase difference between the modes.

B. Methodology of Characterizing the HC-ARPCF

The spectral transmission of antiresonant fibers manifest as multiband transmissions. When a frequency satisfies the resonance condition, light leaks out from the hollow core. Light leakage from the core at the resonance frequency creates a high transmission loss that manifests as a transmission dip.

The resonance frequency (f_{m}) depends on the cladding tube thickness t [49] or η_{clad} or η_{co} and is calculated from the following equation [50]:

$$f_{\text{m}} = \frac{mc}{2t\sqrt{n_{\text{clad}}^2 - n_{\text{co}}^2}} \tag{1}$$

where n_{clad} represents the refractive index of the cladding material, Zeonex, in this work. The n_{co} indicates the refractive indices (RIs) of the core material and m is an integer, representing the order of resonance.

The loss contribution for HC-ARPCFs in terahertz spectrum is the confinement loss that arises when light from the source is not confined to the core region and leaks out toward the cladding. In fiber geometry, leakage can arise when light is trapped into the polymer webs, or in the small gaps between the tubes and the external fiber jacket. In numerical calculations, confinement loss is proportional to the imaginary part of complex refractive index of the guided mode, which can be calculated by [54]

$$L_{\text{c}} = \left(\frac{4\pi f}{c}\right) \text{Im}(\eta_{\text{eff}}) \, \text{cm}^{-1} \tag{2}$$

where L_{c} indicates the confinement loss, f specifies the operating frequency, and $\text{Im}(\eta_{\text{eff}})$ represents the imaginary part of the effective refractive index.

The fraction of power (P) confined in sample area, for example, in core or in the bulk material, is used to quantify the amount of overlap between light and material and it follows as [55] and [56]

$$P = \frac{\int_{\text{sample}} \text{R}_{\text{e}}(E_{\text{x}}H_{\text{y}} - E_{\text{y}}H_{\text{x}}) \, dxdy}{\int_{\text{total}} \text{R}_{\text{e}}(E_{\text{x}}H_{\text{y}} - E_{\text{y}}H_{\text{x}}) \, dxdy} \times 100 \tag{3}$$

where R_{e} denotes the real part, E_{x}, E_{y} and H_{x}, H_{y} are the transverse electric and magnetic field of the guided mode, respectively. For the sensing purpose in this simulation, the integration of the numerator is carried out for the analyte to be sensed in the core region, and the integration of denominator is performed over the whole fiber region.

A second loss mechanism in antiresonant fiber is the effective material loss (EML) (α_{eff}) that is introduced when guided light is absorbed by the background material [54], [57], [58], and is given by

$$\alpha_{\text{eff}} = \sqrt{\frac{\epsilon_0}{\mu_0}} \left(\frac{\int_{\text{mat}} n_{\text{mat}}|E|^2 \alpha_{\text{mat}} dA}{|\int_{\text{all}} S_{\text{z}} dA|} \right) = \alpha_{\text{mat}} P_{\text{mat}} \tag{4}$$

where ϵ_0 and μ_0 designate the permittivity and permeability in free space, n_{mat} indicates the effective refractive index of Zeonex, and S_{z} implies the z-component of Poynting vector, $S_{\text{z}} = \frac{1}{2}(\mathbf{E} \times \mathbf{H}^*)z$, where $\mathbf{E}$ is the electric field component and $\mathbf{H}^*$ is the magnetic field component. The integration in the numerator is only performed over the solid material because the propagation loss of terahertz radiation in air is negligible in comparison. As the material absorption loss is spatially uniform, the α_{eff} is given by the product of material absorption loss and the fraction of power in material (P_{mat}). Here, P_{mat} is calculated with (3) considering the sample being the fiber solid material (Zeonex). The material absorption loss (α_{mat}) is linearly proportional to frequency ranges between 0.2 and 1.6 THz for Topas,

where the α_{mat} is observed 0.06 cm^{-1} at 0.4 THz and it increases at a rate of $0.36 \text{ cm}^{-1}/\text{THz}$ [57]. Using the same concept on Zeonex, the α_{mat} is calculated by $\alpha_{\text{mat}} = 0.36 \times (f-0.4) + 0.06$ cm^{-1}, where f is the frequency in THz. The confinement loss (Lc) is then added to the EML (α_{eff}) to produce transmission loss [38].

$$\alpha_{\text{trans}} = \alpha_{\text{eff}} + L_{\text{c}}. \tag{5}$$

To investigate the refractive index sensing performance, it is important to calculate the relative sensitivity. Relative sensitivity measures the amount of light and sample interaction within the core and can be expressed as [53], [63]

$$R_{\text{s}} = \frac{n_{\text{r}}}{n_{\text{eff}}} \times P_{\text{air}} \tag{6}$$

where Rs is defined as the relative sensitivity, η_{r} is the refractive index of the sample that need to be sensed, η_{eff} represents the effective refractive index in wave guide, and P_{air} is the percentage of light/gas interaction in hollow core calculated from (3).

From the result of relative sensitivity, refractive index sensitivity (S_f) can be calculated by the following equation [64]:

$$S_f = \frac{\Delta_{\text{f}}}{\Delta_{\eta}} \tag{7}$$

where Δ_f represents the spectral shift of the resonance frequency and Δ_{η} is the change of the analytes refractive index.

Another sensor performance parameter called the figure of merit (FOM) evaluates the overall sensing performance of a sensor. The FOM implies the detection limit of the refractive index sensor and is defined as follows [65]–[68]:

$$\text{FOM} = \frac{S_{\text{f}}}{\text{FWHM}} \tag{8}$$

where FWHM denotes the full width at half minima of a resonance dip.

The degree of detection of a sensor can also be measured using the quality factor (Q) that is defined as [69]

$$Q = \frac{f_{\text{m}}}{\text{FWHM}} \tag{9}$$

where f_m is thcy and calculated from (1).

Sensor interaction length is necessary to highlight the sensing performance of a refractive index sensor and is determined from [68]

$$L = \frac{1}{\alpha \text{trans}} \tag{10}$$

L represents the fiber physical length where the input signal will drop to $1/e$ (37%) to its original value, determined from the transmission loss (α_{trans}) using (5).

C. Methodology of Filament Making, 3-D Printing, and Fiber Drawing

Out of many ways of fabricating optical waveguides, recent attention has been directed toward 3-D printing with its ability to produce different symmetric and asymmetric fiber structures, owing to continuous improvements in manufacturing technologies. The idea of 3-D printing fiber first emerged in 2016 [72], where the authors presented the potential of drawing a fiber cane

from a 3-D printed fiber preform using a PMMA filament. In 2017, the first drawn HCF cane was demonstrated [73]; however, no optical guiding was observed.

There are different 3-D printing methods for polymers including stereolithography apparatus (SLA) and fused decomposition modeling (FDM), that constrain the types of base materials that the printer can use. Due to the photocuring process, SLA printing is used for thermoset polymers, while FDM uses thermoplastics such as Zeonex. In 2016, Yang *et al.* [74] investigated 3-D-printed terahertz hollow waveguide based on a Kagome photonic structure using the *Objet30 Prime* printer, which is an SLA printer. The lowest reported loss thorough this fiber was 0.002 cm^{-1} (0.868 dB/m) at 0.75 THz. The core in [74] is massive at 9 mm, with the lengths of 10, 20, and 30 cm. However, thermoset polymers cannot be remelted, and therefore SLA is not a suitable choice for drawing the fiber. Note that FDM methods work for thermoplastic polymers, with a wider variety of available polymers.

As the FDM technique is suitable for fabrication with a wider range of polymers, it is selected for the fabrication of our Zeonex-based fiber samples. The FDM technique is also the most commonly used and low-cost technique. It relies on a polymer filament fed through a nozzle depositing molten polymer that cools and hardens after deposition [30], [75].

The procedure for 3-D printing can be divided into three main steps. In the first stage, the sample filament is made from Zeonex granules. Second, the 3-D-printed fiber is made with a 3-D printer using those filaments. Finally, fiber drawing is performed on the 3-D-printed fiber to obtain the required thickness. The final "fiber drawing" step is optional and is possible to avoid by using a 0.1-mm nozzle diameter delivering a 20-μm layer thickness, even with higher quality printing resolution as mentioned in [77]. Due to the larger wavelength in the terahertz regime compared to visible and infrared, the dimensions of the fiber are much larger. As a result, some of the fibers for short-range terahertz applications can be printed directly using the FDM printer, which can reduce the cost of requiring a drawing tower. The procedures employed in this manuscript for the 3-D printing are explained in Fig. 2(a) and (b).

In this manuscript, we carry out the measurements directly on 3-D printed fiber samples with scaled-up dimensions for the lengths of $L = 8, 20, 30, 40,$ and 50 mm, due to the low resolution of employed 3-D printer. The final stage of fiber drawing remains open for future study, to obtain the numerically optimized dimensions (described in Section II-A). The cross section of the fiber used in our experiment is of $D_{\text{c}} = 5$ mm, $d_{\text{in}} = 1.55$ mm, $t = 0.45$ mm, $w = 1.25$ mm, and $g = 0.811$ mm.

To improve the quality of the filament and fiber, we bake the Zeonex granules at 78 °C over 24 h in an oven. This assists with the reduction of trapped air bubbles in the filament. During heating, air bubbles can expand and create filament deformation and sudden breakage. Additionally, trapped air bubbles can also expand in the fiber during the printing process and degrade the fiber quality. A 3-D filament extruder *Filabot EX2 Filament Extruder* is used to extrude the granules to a 1.76 ± 0.01-mm Zeonex filament at 198 °C, that is compatible with the employed 3-D printer. In this way, we are able to make pure transparent Zeonex filaments without air bubbles.
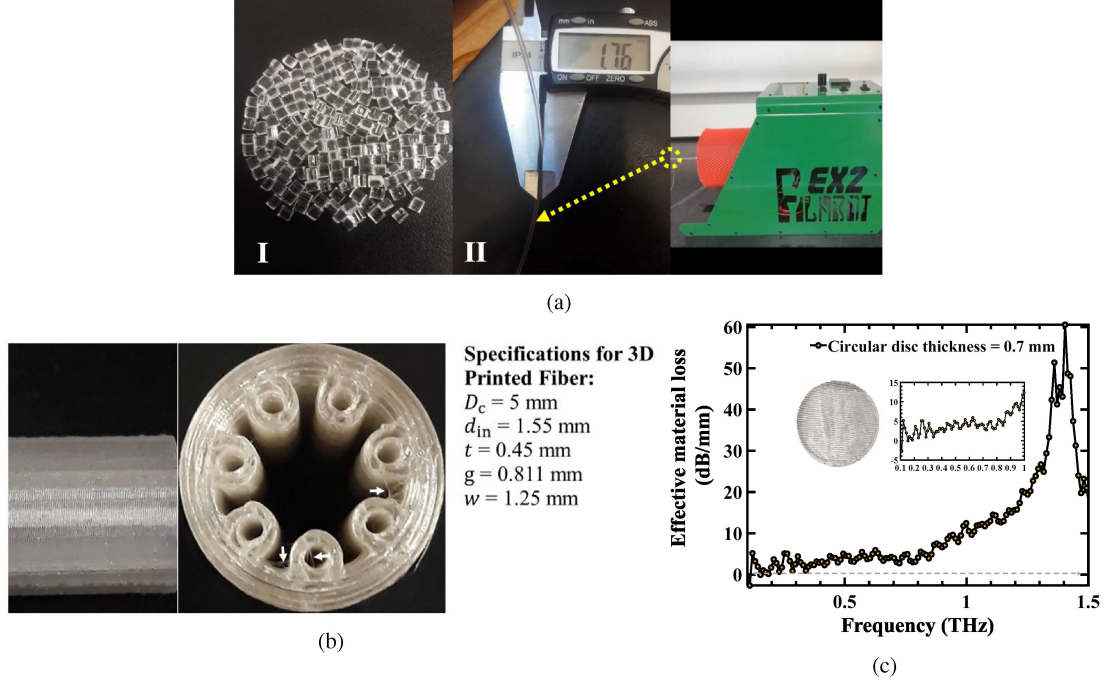
(a)

(b)

(c)

Fig. 2. Preparation of filament and 3-D-printed fiber using that filament. (a)-(i) Zeonex granules (480R) manufactured by Zeon corporation; (a)-(ii) Zeonex filament of 1.75 mm diameter made by *Filabot EX2 Filament Extruder*. (b) side and top views of the 3-D-printed Zeonex fiber (from left to right). The white arrows indicate the unexpected webs. (c) EML measured on a circular disc with a thickness of 0.7 mm and a diameter of 24 mm in the 0.1–1.5 THz.

The 3-D model of the proposed HC-ARPCF fiber is designed using *Autodesk Inventor* Professionals 2019 software and is ported into a stereolithography (STL) file format. The fiber is printed using a *Flashforge Creator Pro*, with a minimum vertical feature size of 0.4 mm and a maximum height of 150 and 0.1 mm horizontal resolution. The fiber transparency is optimized by ensuring that the adjacent printed lines are fused with minimal air trapping. To reduce air-gaps, the amount of trapped air, and the size distribution of the air bubbles from the adjacent printed lines, the infill is set to 100% and the layer height is reduced to as small as possible—rather than using a few larger layers of plastic, we use many smaller but much more tightly packed together layers. The temperatures and speeds that we use are a product of vigorous trial and error. The final temperatures that are settled-on are chosen as they produce the best quality and most consistent prints. For the best results, a nozzle temperature of 273°C is used as well as setting the platform temperature to 125°C. The parts are printed at the slow speed of 8 mm/s to gain the fastest and decent adhesion between the adjacent layers, whereas typical printing speeds are usually in the range of 70–100 mm/s. The HC-ARPCF fiber is then cleaved by using heated razor blade from the 3-D printer and the image of its cross section is presented in Fig. 2(b). We use this fiber as a HC-ARPCF directly for experimental measurement. The deposition of heated liquid Zeonex in Fig. 2(b) may vary the tube thickness a little along its axial direction due to the fluid properties and movement of the nozzle creates unexpected tiny threads near the adjacent gaps and inside the tubes, which need to be cleaned.

To measure the EML of the Zeonex polymer, a circular disc with an uneven thickness of 0.65 ± 0.05 mm and a diameter of 24 mm is printed, as shown at the inset of Fig. 2(c). Fig. 2(c) shows the measured EML in the 0.1–1.5 THz range. The measured EML of the printed Zeonex is about 5 dB/mm, in the 0.1–0.8 THz range, and this increases gradually to 26 dB/mm for 1.3 THz. The unpolished 3-D printed solid surface, which is not fully transparent for terahertz transmission, increases the EML as compared to the transparent Zeonex disc [76] due to the surface scattering loss arising from the coarseness of the printed disc. The measurement details are discussed in Section IV(A).

III. NUMERICAL MODELLING AND SIMULATION

The most challenging task in designing HCFs is to maintain the trade-off between single-mode operation and low transmission loss. Large hollow core allows propagation of light with low transmission loss, but simultaneously introduces modal interference within the core. As the modal interference affects the transmission performance, this section analyzes the characteristics of HOM suppression and transmission losses of the proposed HC-ARPCF.

Antiresonant fiber guides light in the air core due to the antiresonance associated with tiny struts around the core boundary [30], [48]. The guidance is enhanced through the reduced overlap between core and cladding modes, termed as inhibited coupling [23], [24]. The necessary condition to create inhibited coupling between the core and cladding modes for low loss guidance is the specific tube arrangement. To introduce inhibited coupling in our proposed HC-ARPCF, cladding tube structure features a nodeless core boundary and a negative core curvature. The nodeless core boundary means that the tube elements do not touch and help to reduce the loss caused by Fano-resonance [37],
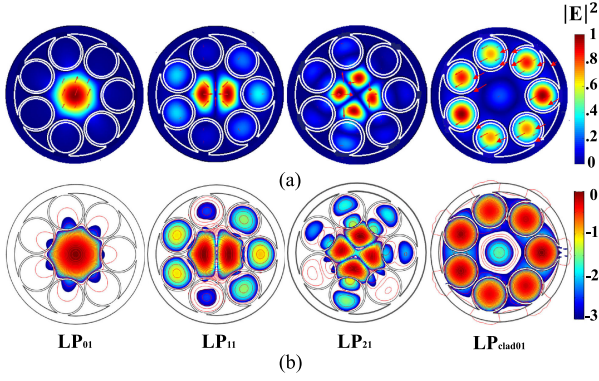
Fig. 3. (a) Simulated mode field profile for fundamental mode (LP_{01}), HOMs (LP_{11}, LP_{21}), and cladding mode (LP_{clad01}) at $d_{in}/D_c = 0.68$ and 1 THz when $D_c = 3$ mm. (b) Logarithmic contour lines of corresponding mode patterns.

while the negative core curvature in which the curvature direction of the tube elements is reciprocal to the core boundary is found to enhance the inhibited coupling between the core and cladding modes [32]. In other words, resonant coupling between core and cladding modes increases the loss. In our HC-ARPCF, we introduce the resonant coupling between higher order core and cladding modes to create a high loss so that mode contamination in core can be suppressed allowing the HC-ARPCF to be effectively single. The procedure to create resonant coupling between higher order core and cladding modes will be discussed more in Section III(A).

Fig. 3(a) represents the mode field intensity of fundamental (LP_{01}) and higher order (HOM: LP_{11} and LP_{21}) core modes, respectively; while cladding mode is denoted as LP_{clad01}. It has numerically shown that modal characteristics are dominated by the first cladding layer, and the increase of the ring number has little influence on the modal properties of the waveguides [49]. Fig. 3(b) highlights the contour lines of the corresponding simulated mode profiles at 1 THz for $d_{in}/D_c = 0.68$ to introduce resonant coupling between HOMs and cladding. A very small fraction of power leaks towards cladding for LP_{01}. The LP_{11} and LP_{21} show strong interaction of power with cladding to introduce higher order suppression.

A. HOM Suppression and Single-Mode Operation

Fig. 4 shows how the resonant coupling effect can be exploited to make the negative curvature HC-ARPCF a single-mode guiding fiber. To determine the resonant point, numerical simulations are performed with $D_c = 3$ mm, $t = 0.09$ mm, and $f = 1$ THz at first transmission window.

In this article, we analyze the effect of inner cladding tube diameter (d_{in}; see Fig. 1) on resonant coupling. The simulations in Fig. 4 are performed with fixed-core diameter (D_c) while we vary the inner tube diameter (d_{in}) as a ratio of d_{in}/D_c from 0.5 to 0.72. It assumes in Fig. 4(a) that the real part of simulated effective indices of LP_{01}, LP_{11}, and LP_{21} are almost constant with the change of d_{in}/D_c at 1 THz where LP_{clad01} increases with the increase of d_{in}/D_c. The LP_{clad01} creates a strong resonant coupling with LP_{11} at $d_{in}/D_c = 0.68$ owing to their phase-matched condition ($n_{eff-LP_{11}} = n_{eff-LP_{clad01}}$).
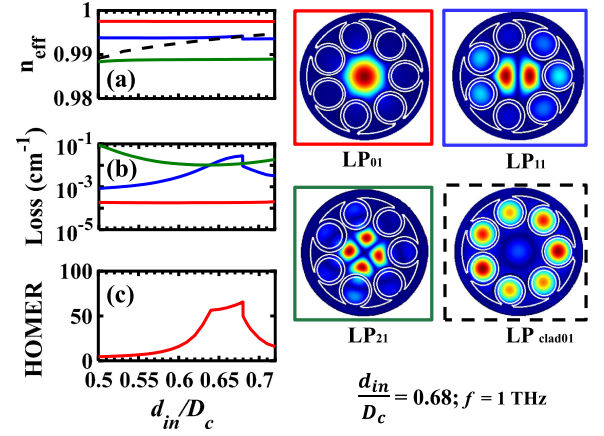

Fig. 4. Effect of changing the inner tube diameter d_{in} on resonant coupling between core modes and cladding mode while core diameter $D_c = 3$ mm. (a) Effective indices (LP_{01}, LP_{11}, LP_{21}, and LP_{clad01}). (b) Transmission loss of core modes. (c) HOMER as a function of d_{in}/D_c. The color of the frame corresponds to the color of line of the plot.

TABLE I
OPTICAL PROPERTIES FOR SEVEN TUBE HC-ARPCF AT 1 THZ

Property	Seven Tube HC-ARPCF
Anti-crossing point	$d_{in}/D_c = 0.68$
Trans. loss of LP_{01}	1.86×10^{-4} cm^{-1}
Trans. loss for LP_{21}	1.2×10^{-2} cm^{-1}
HOMER	66
Optimized trans. loss	1.86×10^{-4} cm^{-1}

As a consequence, strong anti-crossing leads to high transmission loss for LP_{11} mode. Interestingly, the LP_{01} has relatively constant transmission loss with a minimum value of 1.86×10^{-4} cm^{-1} over a wide range of d_{in}/D_c. The lowest transmission loss of HOMs at $d_{in}/D_c = 0.68$ obtained from LP21 is of 1.2×10^{-2} cm^{-1} in Fig. 4(b). The result indicates that HOM suppression is possible with the proper engineering of cladding structure.

In addition, higher order mode extinction ratio (HOMER), which is defined as the ratio between the lowest loss of HOMs and the loss of fundamental mode [33] shown in Fig. 4(c), is used to quantify the single-mode behavior and strong modal filtering. For $d_{in}/D_c = 0.68$, the HOMER is 66. This assures that 66 times lower loss is achieved for LP01 as compared to the lowest loss of core HOM (LP21) when the HC-ARPCF is kept straight.

Table I highlights the optical properties obtained for different modes of the proposed HC-ARPCF. It indicates that, the maximum achievable HOMER is of 66 with $d_{in}/D_c = 0.68$ where obtainable minimum loss is 1.86×10^{-4} cm^{-1}, including material loss.

B. Transmission Loss Spectrum

Fig. 5(a) shows the simulated transmission loss of bare HC-ARF with EML and confinement loss for different frequencies following (2), (4), and (5). The fraction of power (P) inside the polymer web-estimated from (3) is 1000 times smaller than
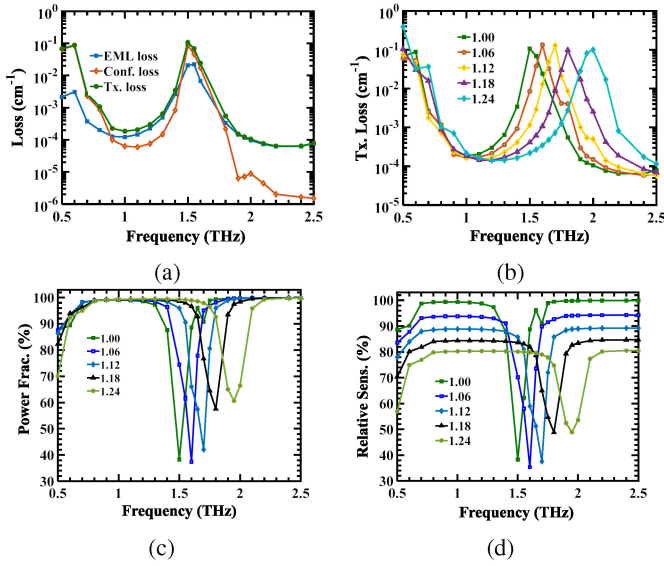
Fig. 5. (a) Loss spectra (EML, confinement loss and transmission loss) of the proposed HC-ARPCF considering the RI of air. (b) Transmission loss spectra with different variation of analyte RI. (c) Core power fraction for different analytes of the proposed gas sensor. (d) Relative sensitivity of the proposed gas sensor.

Fig. 6. (a) Change of resonance frequency with the change of refractive index; (b) FOM and FWHM with RI variation.

the guided core mode—thus, the EML for guided radiation is thousand times lower than the polymer loss in the low loss region. The material absorption loss (α_{mat}) of Zeonex is linearly proportional with frequency [45], [57], [59], [60]. At higher frequencies, the dielectric losses of transparent polymer increases due to polarization relaxation [61], [62]. Hence, the effect of EML is not obvious in the lower frequency region (e.g., lower than 0.9 THz) and, as the frequency increases, the increment in EML will be significant at higher frequencies. Fig. 2(c) experimentally verifies the properties of EML with printed Zeonex disc and the measured EML as a function of frequency follows the similar concept. Fig. 5(a) clearly shows that the transmission loss is unaffected by EML in the frequency range between 0.5 and 0.9 THz. In the first transmission spectrum, a low-loss region appears around at 0.9–1.3 THz and minimum loss of 1.86×10^{-4} cm^{-1} obtained at 1 THz at a transmission bandwidth of 0.5–1.5 THz. The HOM suppression and low transmission loss over large bandwidth of seven-tube HC-ARPCFs suggest that such waveguides can offer an attractive platform for the creation of efficient transmission of terahertz waves.

C. Performance of the Proposed HC-ARPCF as a Sensor

On the basis of guiding properties between Figs. 4 and 5(a), we numerically show the HC-ARPCF sensing performance by changing the RIs from 1.0 to 1.24 in the core at Fig. 5(b). At the resonance frequency (f_{m}), the effective RIs between LPclad01 and LP01 create a resonant coupling, and LP01 experience enhanced leakage through the high-indexed Zeonex layer. The theoretical $f_{\mathrm{m}} = 1.446$ THz is estimated from (1) at $m = 1$. The simulated f_{m} at 1.5 THz shows blue-shift relative to the corresponding theoretical value. The blue shift of the resonance frequency can be explained by the mode field distribution [78].
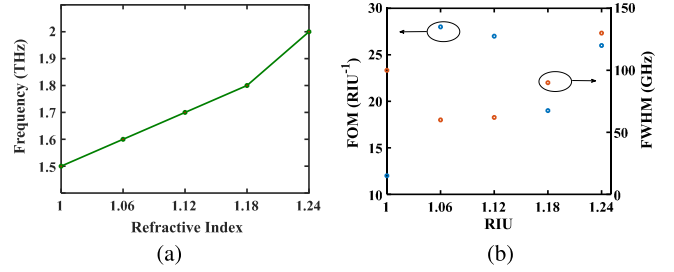
More frequently, changes in real part of RI for LP01 is sensed via resonance peak shifts [79]. Fig. 5(b) indicates that when the refractive index of the hollow core is changed and loaded with the refractive index of 1.06, 1.12, 1.18, and 1.24, the resonance dips from 1.5 THz change their positions and shifts towards 1.6, 1.7, 1.8, and 2 THz, respectively. These resonant shifts are the signature of refractive index variation inside the fiber core, demonstrating how the fiber can potentially be an effective and sensitive refractive index transducer. Fig. 5(c) shows the amount of light and analyte interaction of the fundamental LP01 mode within the guided hollow core for different analytes as a function of frequency, obtained from eigen mode solver using (3). The numerical simulation reveals that more than 98% of power concentrates within the hollow core for this propagation mode around 1 THz. The increase of n_{co} reduces the difference between the n_{clad} and n_{co}, which in turn disturbs the guidance of light using ARROW model and may suppress the resonant properties of the fiber. In this case, most of the light will be guided through the core due to small index variations between core and cladding, and the core power fraction may gradually increase with the analyte refractive index at the resonant frequency. The modal power distributions by means of different effective RIs of the core filled with analytes correspond to the spectral characteristics of analytes. Fig. 5(d) represents the relative sensitivity calculated from (6) of the RI sensor. Specifically, transmission dips are considered for analyte species characterization because it is rarely affected by the analyte pressure, analyte temperature, or system's dynamic range as is the absorption strength. Relative sensitivities of the proposed terahertz refractive index sensor are 38, 35, 37, 48, and 49 at the transmission dips for an analyte RI of 1.00, 1.06, 1.12, 1.18, and 1.24, respectively.

Fig. 6(a) illustrates the relationship between the analyte RI and the corresponding resonant frequency. In this simulation, the transmission dip goes to higher frequencies with increase in analyte refractive index. In other words, the relationship between the small change of refractive index in the core and slight shift of resonance frequency is linear to a first-order approximation. In our analysis, the resonance frequency is at 1.5 THz for RI of 1.0 and the FWHM of the resonant peak is about 0.1 THz. For the next step, the analyte RI of 1.0 is replaced with 1.06, 1.12, 1.18, and 1.24, and the corresponding FWHMs are 0.06, 0.062, 0.09, and 0.13 THz, respectively. The increase in resonance bandwidth (FWHM) can be used to detect higher RIs. As can be seen from Fig. 6(a), the simulated refractive index

TABLE II
TERAHERTZ SENSING PERFORMANCE OF THE PROPOSED ANTIRESONANT FIBER

Analyte refractive index variation	Resonant peak (THz)	Relative Sensitivity (S_f)	Refractive index sensitivity (GHz/RIU)	FWHM (GHz)	Quality factor	FOM (RIU^{-1})	Length (cm)
1.00–1.06	1.5	38	1670	100	15	17	9.4
1.06–1.12	1.6	35	1670	60	27	28	7.7
1.12–1.18	1.7	37	1670	62	27.5	27	7.7
1.18–1.24	1.8	48	1670	90	20	19	10
1.24	2.0	49	3335	130	16	26	10

change of $\Delta\eta = 0.06$ results in a resonance frequency shift of $\Delta f = 100$ GHz for RIs between 1.00 and 1.18, and 200 GHz for refractive indices from 1.18 to 1.24. The constant spectral shift $\Delta f = 100$ GHz for the constant refractive index variation $\Delta\eta = 0.06$ results in the relative sensitivity 1670 GHz/RIU, as shown in Fig. 6(a). However, the change in spectral shift $\Delta f = 200$ GHz at 1.24 has doubled the relative sensitivity. The unspecified mode confinement at resonance frequency can create impact on the transition of resonant frequency toward 2 THz with spectral shift $\Delta f = 200$ GHz and doubles the theoretical refractive index sensitivity $S_f = 3333$ GHz/RIU for 1.24. From (7), the theoretical refractive index sensitivity (S_f) for the proposed sensor is from 1670 to 3335 GHz/RIU.

The proposed sensor shows FOMs of 17, 28, 27, 19, and 13, respectively. The highest FOM is obtained for the refractive index of 1.06, as shown in Fig. 6(b), as the resonance bandwidth (FWHM) is comparatively sharper than at this value.

A high-quality factor (Q) sensor implies high sensitivity and a narrow FWHM [69]. The Q values of the proposed refractive index sensor are 15, 27, 27.5, 20, and 16, respectively.

Sensor length is also an important parameter that is determined from the inverse of the transmission loss. As the transmission loss characteristics in HC-ARPCF varies with different refractive indices, the sensor lengths also vary accordingly. The transmission losses at resonant points are 0.11, 0.13, 0.13, 0.1, and 0.1 cm^{-1} for refractive indices of 1.00, 1.06, 1.12, 1.18, and 1.24, respectively. At the resonance frequencies, maximum fiber operating lengths range between 7.7 and 10 cm.

For the variation of analyte refractive indices, Table II shows the performance metrics of the proposed terahertz refractive index sensor that indicate that, with the change of refractive index, the proposed sensor can attain a maximum spectral sensitivity of 3335 GHz/RIU, and maximum quality factor and FOM of 27.5 and 28, respectively.

The large effective refractive index variations in an analyte cell can easily be detected via the time of arrival. This analyte detection method employs incoherent Fourier transform infrared system or coherent time-domain terahertz system and is a known spectroscopic method in analyte sensing. This spectroscopic method is based on the signature as a function of frequency or 'fingerprint' of absorption of molecules in the terahertz regime [4]. Due to weak absorption by gases in the terahertz region and poor signal-to-noise ratio, an extremely long gas cell (few meters) is required to increase the interaction length and to detect absorption lines of gases reliably. The second method for analyte sensing is based on the phase matching of resonant structure such as a terahertz whispering-gallery mode (WGM) resonator [70], [71], a 1-D cavity-based photonic crystal fiber on

silica slab [64], a 2-D photonic crystal resonator based on pillar arrays [80], and a surface plasmon resonance-like polymeric fiber based on a porous core [81]. While the FOM and the Q value might be reasonable for different types of terahertz integrated devices, such as WGM resonators and surface plasmon resonance-based fiber sensors, they are not discussed in this manuscript due to difficulties in coupling, their very short interaction length, and complex fabrication techniques that can limit their analyte sensitivity and selectivity for a larger target than the sensor chip. They detect analytes via resonance frequency shifts via a time-domain terahertz system.

The terahertz sensing capabilities of antiresonant fiber [31], [82], [87] and PBG waveguides [88], [89] are also relevant to resonant structures. They can detect the target analyte via the shift of resonance frequency and their interaction lengths can cover a few centimeters. Among them, [82], [87] are fabricated with fiber drawing procedure and the rest of them [31], [82], [87] are fabricated with fiber drawing procedure. In [82], the authors add liquids such as water, hydrochloric acid, acetone, and ammonia in a dielectric pipe waveguide and let them to evaporate. When measuring the change in the transmission power, they inferred the effective RIs to be in the range of 1.016–1.102. Sensing the vapor instead of the liquid itself can be an interesting option when dealing with high loss liquids in the terahertz regime such as water 200 cm^{-1} [83]–[85] and acetone 190 cm^{-1} [86] at 1 THz. Vapor sensing has wider real-life application, giving rise to the interest in studying the low refractive index range. The composite and polyvinylchloride porous cladding layer of the same waveguide [82] is applicable for mixed powders (melamine and tryptophan) sensing in the 1.354–1.489 RI range. The best refractive index sensitivity for powder sensing is 22.2 GHz/RIU. The RI of melamine and tryptophan are 1.76 and 1.10, respectively.

Cruz *et al.* [31], [87] proposed a PMMA-based coreless waveguide and a 3-D-printed elliptical-shaped ARF, which can sense the liquid analyte in the 1.4–1.5 and 1.0–1.44 ranges, respectively. The corresponding refractive index sensitivity is 5 GHz/RIU [87] and 972 GHz/RIU [31]. A terahertz SLA-based circular Bragg waveguide sensor in [88] has been used for detecting PMMA films with different thicknesses loaded on the inner surface of the waveguide core, and a surface sensitivity of 0.1 GHz/μm is experimentally achieved. Also, the thickness variation of the α-lactose monohydrate powder analyte with the RI of 1.78 was measured with a change in resonant dips. To disperse the uniform powder thickness in the waveguide core, a motor was attached to apply a centrifugal force in the waveguide.

Later, a mixture of liquid analytes with RI ranges between 1.465 and 1.545 was measured with the FDM-based rectangular

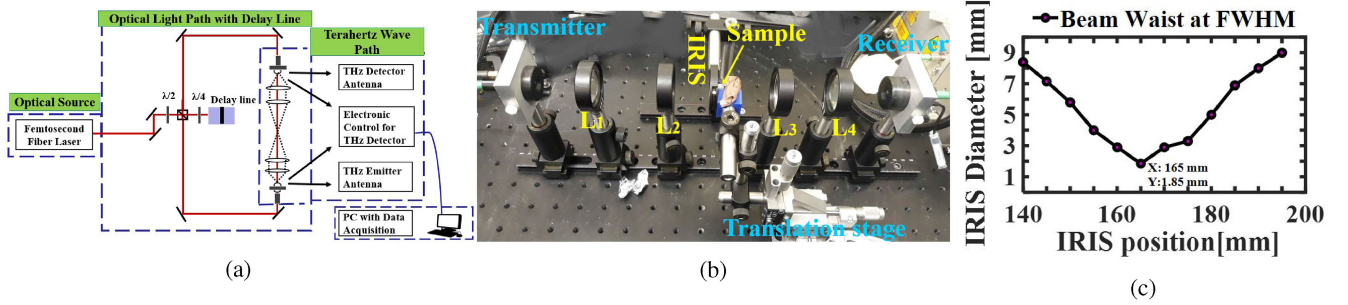| Ref. Sensor resolution	Sensor structure	Refractive index	Average refractive index sensitivity (GHz/RIU)	Quality factor	FOM (RIU^{-1})
A. Cruz, [87]	Core-less wave guide	1.4–1.5	5	-	-
A. Cruz, [31]	Hollow pipe wave guide	1.0–1.44	972	-	-
This Paper	Seven tube HC-ARPCF	1.00–1.24	from 1670 to 3335	from 15 to 27.5	from 17 to 28

Fig. 7. (a) Schematic diagram of terahertz time-domain spectroscopy system. (b) Setup for the terahertz experiment: terahertz transmitter, L_1, L_2, IRIS, fiber under test, L_3, L_4, terahertz detector (from left to right in bottom). Terahertz time-domain spectrometer here: Menlo system (TERA K15 Terahertz Kit). (c) Beam diameter between L_2 and L_3, measured with IRIS.

Bragg waveguide [89]. The refractive index sensitivity and the sensor resolution of the terahertz Bragg waveguide-based fluidic sensor are measured to be 110 GHz/RIU and 4.5×10^{-3} RIU, respectively. The liquid mixtures were formed using mineral oil (1.455) and cinnamon essential oil (1.555). In this manuscript, our proposed seven-tube HC-ARF can numerically detect the analyte, with the RI ranges ranges between 1.00 and 1.24 are in the group of vapor as considered in [82]. The resultant refractive index sensitivity, quality factor, and FOM range from 1670–3335 GHz/RIU, 15–27.5, and 17–28 RIU^{-1}.

The performance of the proposed sensor as compared with the prior sensors reported for terahertz sensing is shown in Table III. Based on the average sensitivity, quality factor, and FOM, the proposed sensor shows improved performance.

IV. EXPERIMENTAL SETUP AND CORRESPONDING RESULTS

A. Experimental Setup

A THz-TDS system with photoconductive antennas as transmitter and receiver, and four plano-convex, aspheric lenses made of TPX polymer [91] are used for fiber characterization. We perform the transmission measurements of Zeonex-based seven-tube HC-ARPCF using a commercial fiber-coupled THz-TDS system (Menlo) with an effective spectral range of 0.1–2.0 THz.

The schematic diagram for terahertz fiber transmission using Menlo system is shown in Fig. 7(a). The THz-TDS system consists of three main parts: 1) optical source, 2) delay line controller, and 3) terahertz wave path. The laser beam generated from "T-light" (optical source) is split into a strong pump beam for the generation of the terahertz radiation and a weak probe beam for the detection. The terahertz pulse, generated from the LT-GaAs-based photoconductive antenna, is collimated by an on-axis plano-convex lens (L_1) to produce a nearly parallel

beam with Gaussian FWHM of 25 mm. Another plano-convex lens (L_4) is used to focus the collimated terahertz beam on the terahertz detector antenna.

The detector antenna is gated by the optical probe beam, and the current, which is proportional to the incident terahertz field, is recorded using a lock-in amplifier as a function of the temporal delay between the pump and probe beams. An acousto-optic modulator allows the pump beam to be modulated at a frequency of 10 kHz, where the system has the highest signal-to-noise ratio. Prior to the HC-ARPCF loss measurement, another pair of on-axis plano-concave lenses (L_2 and L_3) with the focal length of 50 mm are placed between the collimated terahertz beam to couple the beam waist into the hollow core of HC-ARPCF, which is important for fundamental mode matching. The plano-convex lenses (L_2 and L_3) focus the beam to a 1.85-mm waist verified by an IRIS, shown in Fig. 7(c). These two plano-convex lenses are separated by 100 mm, as the focal lengths are 50 mm. The spectrometer is set to operate in rapid scan mode, with a lock-in time constant of 300 μs for observing alignment and signal properties during the measurement setup. Then, a lock-in time constant of the 10 ms is selected for collecting the data for later analysis. Fig. 7(b) indicates the experimental alignment of terahertz wave path. There are two types of reference signals: i) no fiber and ii) with shortest length of fiber. The 'no-fiber' reference signal is measured without the HC-ARPCF while the sample fiber scan is taken after inserting the fiber sample between the pair of plano-convex lenses (L_2 and L_3) as shown in Fig. 7(b). Here, the IRIS is used to mark the position of beam waist and block any unwanted signal passing through the fiber core.

The transmitted terahertz signal from HC-ARPCF is again collected from another plano-convex lens (L_4) and coupled into a photoconductive detector for terahertz wave measurement.
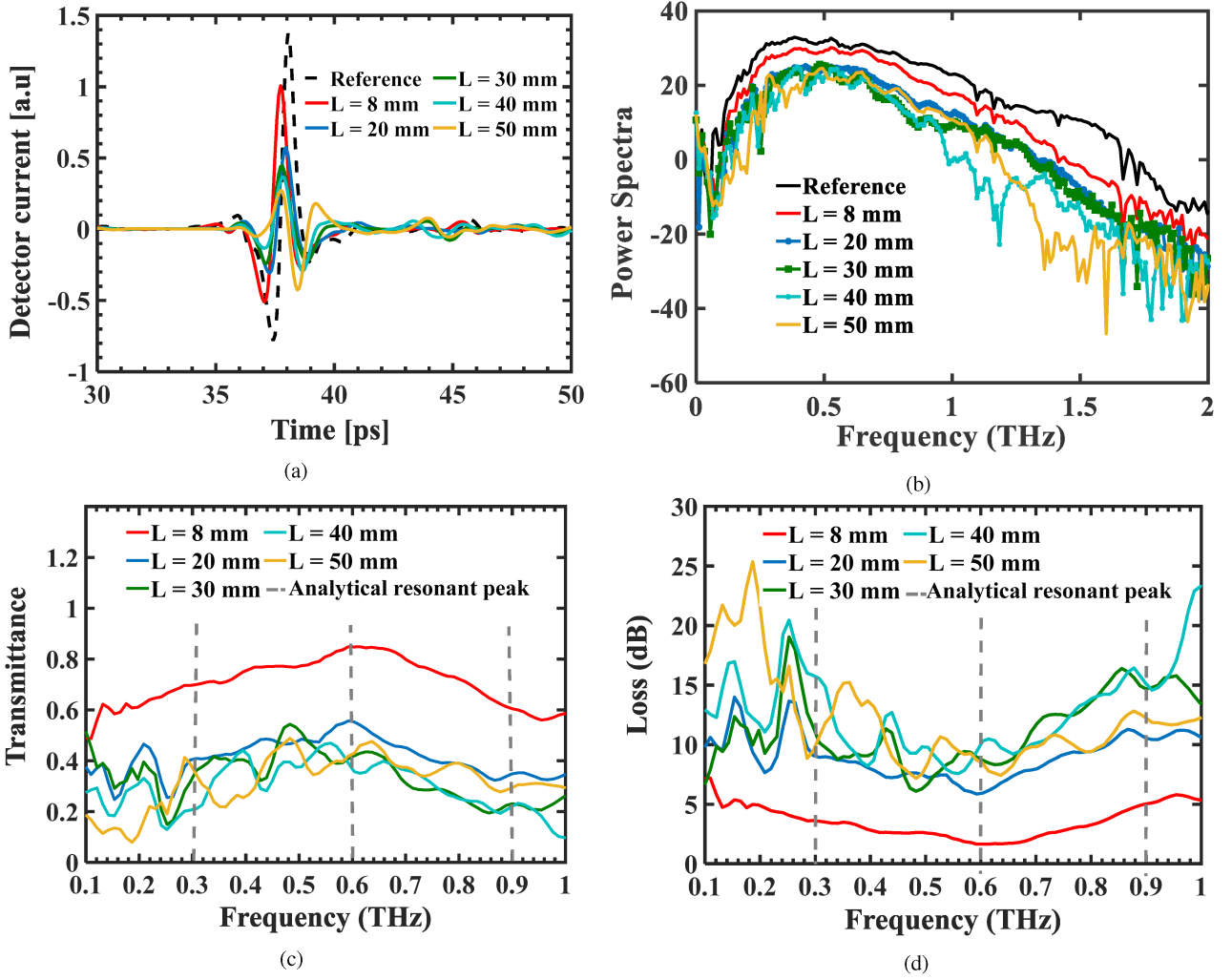
Fig. 8.   (a) Temporal signals as measured by the lock-in amplifier for the reference pulse and sample pulses of the seven-tube HC-ARPCF for the length of $L = 8$, 20, 30, 40, and 50 mm. (b) Corresponding power spectra. (c) Measured transmittance of terahertz HC-ARPCF. (d) Loss measurement of terahertz HC-ARPCF. Vertical grid lines in (c) and (d) denote the theoretical resonance frequencies. All the samples are printed with same capillary thickness and gap between two capillaries of $t = 0.45$ mm and $g = 0.811$ mm.

Both the emitter and detector are pumped with T-light fiber-coupled femtosecond fiber laser. The printed fiber is mounted on an automated xyz-translation stage for mapping the fiber modes. Finally, data acquisition is carried out with "K15 TeraScan Mark II 1.31" software from Menlo. This software provides the temporal and power spectra of the signals for further signal characterization.

B. Experimental Results: Effect of Fiber Length

The experiment is performed with scaled-up dimensions as *Flashforge Creator Pro* can print with a minimum vertical feature size of 0.4 mm. A more optimized fiber can be prepared by drawing the printed fiber [75], [92]. Drawing the fiber to obtain the proposed numerical dimensions can be our future work for the application of analyte sensing.

The 3-D-printed seven-tube HC-ARPCF and corresponding resulting waveforms are shown in Figs. 2(b) and 8, respectively. To characterize the fiber transmission and coupling loss

individually, loss measurement is performed using a cutback technique. It is not possible to cut the printed fiber length during the measurement without changing the coupling conditions as the air holes may collapse during the cutting and need a very high-pressure air purger to remove the obstacles. To avoid this difficulty, we print different lengths ($L = 8$, 20, 30, 40, and 50 mm) of fibers with the same cross section. For guiding the light through the core only, we wrap the individual fiber with aluminum foil with a hole diameter of approximately 5 mm to the input and output waveguide end. We place each length of fiber consecutively in the sample holder, and compare and analyze the effect of length on the terahertz transmission spectrum. Therefore, we cannot assure the coupling loss is constant. Humidity in the air can create water lines in the signal, which decreases terahertz transmission [93]. To study the individual fiber performance accurately, measurements are made in a nitrogen environment with negligible humidity. Also, five scans are performed for each fiber *in situ* and then averaged.

Fig. 8(a) plots the temporal signal of the reference scan and sample scans. The peak of the detector current for reference signal at maximum ranges from -0.78 to $+1.37$ a.u. It decreases gradually from $+1.0$, $+0.58$, $+0.45$, and $+0.37$ to $+0.27$ a.u with increasing the terahertz fiber lengths of $L = 8$, 20, 30, 40, and 50 mm, respectively. The propagation loss introduced by each length of terahertz fiber results in a reduction of peak amplitude of detector current. As seen in Fig. 8(a), the reference signal peak leads by 0.32 ps with respect to the signals through the hollow core fibers. Any small change in alignment can make a difference of arrival time of the transmitted signal through the hollow core. Here, the arrival time difference can arise as we move L_3 toward L_4 to place the fiber end at the probable focal spot of L_4. Also, the time difference may arise from the unexpected webs at the gap between the two adjacent tubes introduced by the FDM printing. This small variation of time delay confirms that most of the terahertz signal passes through the air core with proper alignment.

The power spectra calculated by fast Fourier transform determines the transmission properties of the fiber in Fig. 8(b). The Fourier transform of the recorded detector current of the reference (without the sample) and that through the fibers are used to measure the power spectra for the fibers in each case. We found that there are sudden peaks in samples for $L = 20$, 30, 40, and 50 mm to correspond the resonance frequency. The fiber of $L = 8$ mm carries the similar behaviour of reference signal due to the short fiber length and rarely showing the antiresonant characteristics. Therefore, it is important to have a longer fiber length in order to achieve the characteristics of the fiber and stable mode distribution.

The transmittance of the fiber measured is determined from the absolute ratio (sample and reference) of the complex modulus of the transformed data for different fiber lengths. The measurements on transmittance are taken by comparing the transmitted terahertz waveforms with and without the sample in Fig. 8(c) at the terahertz beam path. The $L = 8$ mm fiber is too short to be called a fiber. A fiber length of 8 mm is not sufficient to draw any conclusions as it is far too short to achieve a stable mode distribution or eliminate others spurious effects. To be clear, the lens focal length is 50 mm maximum. The distance between L_3 toward L_4 is not large enough to place a fiber of $L = 50$ mm while maintaining the proper coupling at the end facet at $L = 50$ mm. Therefore, leaving out the experimental results for $L = 50$ mm may alleviate the coupling problem. However, avoiding $L = 8$ and 50 mm also would mean not giving the full picture regarding the transmission. Fig. 8(d) shows the measured loss. This can be seen clearly in Fig. 8(c) and (d) where $L = 8$ mm seems to be an outlier, when compared to all the other lengths. The $L = 50$ mm fiber is used with a different alignment. By looking at the results of the three remaining fibers, there is hardly any recognizable trend. To assist rigor in the data processing, we attempt to separate the fiber transmission loss from the coupling loss as a combination of different fiber lengths in Fig. 9. In addition, using the 'no-fiber' measurements as a reference can assist with a mixture of coupling efficiency and fiber losses. The 8-mm fiber length is far too short as stated above. The use of a 20-mm-long section as a reference

and comparing this with other fiber lengths may eliminate the coupling loss. The combination of cases that have been chosen are as follows:

a) $L = 8$, 20, 30, 40, and 50 mm; reference = no fiber;
b) $L = 8$, 20, 30, and 40 mm; reference = no fiber;
c) $L = 20$, 30, and 40 mm; reference = no fiber; and
d) $L = 30$ and 40 mm; reference = 20 mm.

In all cases, the fibers are short due to the experimental setup limitation where we were able to measure fibers no longer than 50 mm. To obtain a stable mode distribution inside the fiber considering the excitation of HOMs, it is necessary to have a longer fiber so that the mode distribution can stabilize.

From the transmission loss spectra in Fig. 9(a)–(d)-(i) we can observe that case (a) does not provide the resonance properties at higher frequency. The high and low loss regions can easily be obtained in cases (b)–(d). The analytical resonance peaks for $t = 0.45$ mm appear at ~0.30, ~0.60, and ~0.90 THz, using (1) and the vertical grid lines are the indication of the analytical resonant properties in fiber. The measured resonance peaks for Fig. 9(b)–(d)-(i) appear at 0.31, 0.61, and 0.99 THz, which are almost similar to the analytical results. Moreover, the simulation of the scaled-up fiber is compared here with the measured transmission loss in Fig. 9(a)–(d)-(i). There are some additional losses such as water absorption loss and scattering loss, in addition to the transmission loss, which are introduced during experiments, while neglected during simulations. The low loss of 0.3 dB/mm at 0.47 THz is obtained with case (b). The lowest transmission loss of 0.04 dB/mm is obtained from cases (c) and (d) around 0.53 THz. Fig. 9(c) and (d)-(i) shows a similar trend between simulated and measured transmission loss. We hypothesize that the anti-crossing between fundamental and HOMs may cause high loss peak in the low-loss regions and they are more pronounced at lower frequency around 0.44 THz.

To quantitatively assess the data, we use the linear coefficient errors for transmission and coupling loss based on using the coefficient of determination (R^2) in Fig. 9(a)–(d)-(ii and iii). We plot the coupling and transmission loss when R^2 is higher than 0.6 to obtain reliable data. It is apparent from Fig. 9(a)–(d)-(iii) that the coupling losses vary for different length combinations as the fibers are independent during the measurement. Therefore, it is difficult obtaining constant coupling loss as it ranges from -53 to 15 dB from sample to sample, in the 0.3–1.0 THz. The differences in coupling losses come from the focal spot size mismatch between the fiber front-end facets and adjacent lens due to the consecutive placement of fibers. However, with the help of xyz-translation stages, the radial and lateral displacement has been tried to mitigate. The linear curve fitting over the experimental data in Fig. 9(a)–(d)-(iv) for a few frequencies differentiate the good from poor data. Note that some of the nonidealities in the experimental results are obviously due to the surface roughness of the fiber produced during 3-D printing.

Table IV shows in detail the characteristics comparison of the proposed HC-ARPCFs and investigates the variation in optical performances with prior established results. On the basis of fabrication feasibility, small core size, broad transmission window, and low transmission loss, the obtained results are comparable with the prior results.
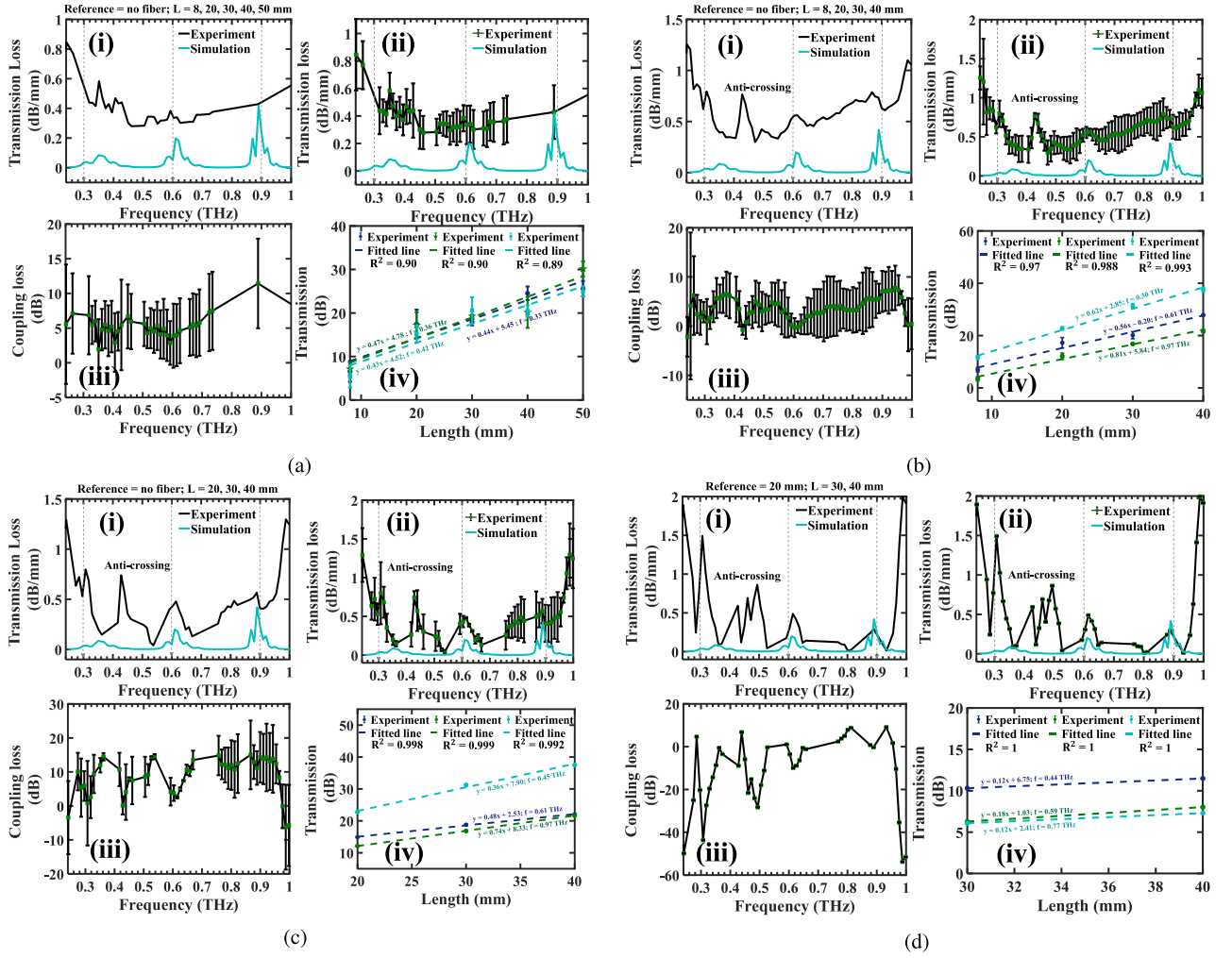
Fig. 9. (a–d)-(i) Frequency-dependent experimented and simulated transmission loss. (a–d)-(ii) Frequency-dependent experimented and simulated transmission loss with their corresponding errors. Vertical grid lines in (i) and (ii) are the indication of the theoretical resonance frequencies of the seven tube HC-ARPCF for the different length combinations. (a–d)-(iii) Frequency-dependent measured coupling loss with corresponding errors;. (a–d)-(iv) Length-dependent transmissions through the HC-ARFs. The solid markers indicate the measured transmission while the dashed lines denote the best-fit lines at different frequencies. All the samples are printed with same capillary thickness and gap between two capillaries of $t = 0.45$ mm and $g = 0.811$ mm, respectively.

TABLE IV
CHARACTERISTICS OF 3D-PRINTED HC-ARPCF-BASED TERAHERTZ FIBER

Ref.	No. of tubes	Material, printing	Core diameter, D_c (mm)	Strut thickness, t (mm)	Total size, OD (mm)	Frequency range (THz)	Transmission loss
J. Yang, [74]	Kagome hollow core	VeroWhitePlus (SLA)	9	0.35	–	0.2–1.0	0.02 cm^{-1} (average)
S. Yang, [94]	Pentagram hollow core	Photosensitive resin (SLA)	-	1	21	0.5–2.0	0.025 cm^{-1} (1.94 THz)
L. D. V. Putten, [30]	6 (Half-elliptical)	Polycarbonate (FDM)	6, 6, 10	0.6, 0.6, 1.2	–	0.15–0.6	–
A. L. S. Cruz, [31]	10 (Elliptical)	ABS polymer (SLA, FDM)	-	0.4, 0.2	8.3	–	–
A. L. S. Cruz, [32]	8 (Cone shaped)	ABS polymer (SLA)	8.4	0.54	25	0.1–0.5	–
This manuscript	7 (Circular)	Zeonex (FDM)	5	0.45	11.8	0.24–1.0	0.04 dB/mm (0.53 THz)

V. CONCLUSION

In this article, an optimized seven-tube HC-ARPCF is analyzed numerically. The optimized dimensions of the fiber provide small spatial overlap between core and cladding modes that facilitates suppressing the HOMs. In the fiber design, a negative curvature of the core boundary has been applied to enhance the inhibited coupling. Moreover, nontouching antiresonant tubes are added to reduce the EML and Fano resonances that may introduce from the connecting nodes. The numerical investigation of the fiber shows a low-loss region within 0.8–1.4 THz and a transmission bandwidth within 0.5–1.5 THz.

The experimental validation of the HC-ARPCF is carried out using THz-TDS where five different fiber lengths were considered to achieve the antiresonant properties. It is found that printed fibers with different fiber length combinations show improved antiresonant effects, and the analytical resonance frequencies are ideally matched with the numerical analysis of scaled-up fiber. Note that there are imperfections in the obtained results which are due to the surface roughness in fiber fabrication. The simplicity in fiber design and appropriate optical properties of the fiber make it a suitable candidate for short-distance terahertz transmission and further can be used for refractometric sensing.

REFERENCES

[1] G. Gallot, S. P. Jamison, R. W. McGowan, and D. Grischkowsky, "Terahertz waveguides," *J. Opt. Soc. Am. B*, vol. 17, no. 5, pp. 851–863, 2000.

[2] S. Atakaramians, A. V. Shahraam, T. M. Monro, and D. Abbott, "Terahertz dielectric waveguides," *Adv. Opt. Photon.*, vol. 5, no. 2, pp. 169–215, 2013.

[3] P. H. Siegel, "Terahertz technology in biology and medicine," *IEEE Trans. Microw. Theory Techn.*, vol. 52, no. 10, pp. 2438–2447, Oct. 2004.

[4] D. M. Mittleman, R. H. Jacobsen, R. Neelamani, R. G. Baraniuk, and M. C. Nuss, "Gas sensing using terahertz time domain spectroscopy," *Appl. Phys. B*, vol. 67, no. 3, pp. 379–390, 1998.

[5] E. Gerecht, K. O. Douglass, and D. F. Plusquellic, "Chirped-pulse terahertz spectroscopy for broadband trace gas sensing," *Opt. Express*, vol. 19, no. 9, pp. 8973–8984, 2011.

[6] H. Lin, W. Withayachumnankul, B. M. Fischer, S. P. Mickan, and D. Abbott, "Gas recognition with terahertz time-domain spectroscopy and spectral catalog: A preliminary study," *Proc. SPIE Terahertz Photon.*, vol. 6840, 2007, Art. no. 68400X.

[7] E. Pickwell and V. P. Wallace, "Biomedical applications of terahertz technology," *J. Phys. D: Appl. Phys.*, vol. 39, pp. R301–R310, 2006.

[8] L.-J. Chen, H.-W. Chen, T.-F. Kao, J.-Y. Lu, and C.-K. Sun, "Low-loss subwavelength plastic fiber for terahertz waveguiding," *Opt. Lett.*, vol. 31, no. 3, pp. 308–310, 2006.

[9] M. S. Islam *et al.*, "Extremely low material loss and dispersion flattened Topas based circular porous fiber for long distance terahertz wave transmission," *Opt. Fiber Techn.*, vol. 34, pp. 6–11, 2017.

[10] M. S. Islam *et al.*, "Porous core photonic crystal fibre for ultra-low material loss in THz regime," *IET Commun.*, vol. 10, no. 16, pp. 2179–2183, 2016.

[11] A. Hassani, A. Dupuis, and M. Skorobogatiy, "Low loss porous terahertz fibers containing multiple subwavelength holes," *Appl. Phys. Lett.*, vol. 92, 2008, Art. no. 071101.

[12] Z. Wu, W-R. Ng, M. E. Gehm, and H. Xin, "Terahertz electromagnetic crystal waveguide fabricated by polymer jetting rapid prototyping," *Opt. Express*, vol. 19, no. 5, pp. 3962–3972, 2011.

[13] K. Nielsen, H. K. Rasmussen, P. U. Jepsen, and O. Bang, "Porous-core honeycomb bandgap THz fiber," *Opt. Lett.*, vol. 36, no. 5, pp. 666–668, 2011.

[14] J. Anthony, R. Leonhardt, S. G. Leon-Saval, and A. Argyros, "THz propagation in Kagome hollow-core microstructured fibers," *Opt. Express*, vol. 19, no. 19, pp. 18470–18478, 2011.

[15] H.-W. Chen *et al.*, "Subwavelength dielectric-fiber-based THz coupler," *J. Lightw. Technol.*, vol. 27, no. 11, pp. 1489–1495, 2009.

[16] B. You *et al.*, "Subwavelength film sensing based on terahertz antiresonant reflecting hollow waveguides," *Opt. Express*, vol. 18, no. 18, pp. 19353–19360, 2010.

[17] L. Vincetti and V. Setti, "Confinement loss in Kagome and tube lattice fibers: Comparison and analysis," *J. Lightw. Technol.*, vol. 30, no. 10, pp. 1470–1474, 2012.

[18] L. Vincetti and V. Setti, "Extra loss due to Fano resonances in inhibited coupling fibers based on a lattice of tubes," *Opt. Express*, vol. 20, no. 13, pp. 14350–14361, 2012.

[19] Y. Y. Wang, N. V. Wheeler, F. Couny, P. J. Roberts, and F. Benabid, "Low loss broadband transmission in hypocycloid-core Kagome hollow-core photonic crystal fiber," *Opt. Lett.*, vol. 36, no. 5, pp. 669–671, 2011.

[20] S. Shuai *et al.*, "Optically pumped gas terahertz fiber laser based on gold-coated quartz hollow-core fiber," *Opt. Express*, vol. 58, no. 11, pp. 2828–2831, 2019.

[21] L. Vincetti and V. Setti, "Extra loss due to Fano resonances in inhibited coupling fibers based on a lattice of tubes," *Opt. Express*, vol. 20, no. 13, pp. 14350–14361, 2012.

[22] F. Benabid, J. C. Knight, G. Antonopoulos, and P. S. J. Russell, "Stimulated Raman scattering in hydrogen-filled hollow-core photonic crystal fiber," *Science*, vol. 298, no. 5592, pp. 399–402, 2002.

[23] A. Argyros and J. Pla, "Hollow-core polymer fibers with a Kagome lattice: Potential for transmission in the infrared," *Opt. Express*, vol. 15, no. 12, pp. 7713–7719, 2007.

[24] B. Debord *et al.*, "Ultralow transmission loss in inhibited-coupling guiding hollow fibers," *Optica*, vol. 4, no. 2, pp. 209–217, 2017.

[25] F. Couny, F. Benabid, and P. S. Light, "Large-pitch Kagome-structured hollow-core photonic crystal fiber," *Opt. Lett.*, vol. 31, no. 5853, pp. 3574–3576, 2006.

[26] J.-Y. Lu *et al.*, "Terahertz air-core microstructure fiber," *Appl. Phys. Lett.*, vol. 92, 2008, Art. no. 064105.

[27] L. Vincetti, "Single-mode propagation in triangular tube lattice hollow core terahertz fiber," *Opt. Commun.*, vol. 283, no. 6, pp. 979–984, 2010.

[28] J. Sultana *et al.*, "Terahertz hollow core antiresonant fiber with metamaterial cladding," *Fibers*, vol. 8, no. 2, pp. 979–984, 2020.

[29] J. Sultana *et al.*, "Exploring low loss and single mode in antiresonant tube lattice terahertz fibers," *IEEE Access*, vol. 8, pp. 113309–113317, 2020.

[30] L. D. Van Putten, J. Gorecki, E. Numkam Fokoua, V. Apostolopoulos, and F. Poletti, "3D-printed polymer antiresonant wave-guides for short-reach terahertz applications," *Appl. Opt.*, vol. 57, no. 14, pp. 3953–3958, 2018.

[31] A. L. S. Cruz *et al.*, "Exploring THz hollow-core fiber designs manufactured by 3D printing," in *Proc. Int. Microw. Optoelectron. Conf.*, 2017.

[32] A. L. S. Cruz, V. A. Serrão, C. L. Barbosa, and M. A. R. Franco, "3D printed hollow core fiber with negative curvature for terahertz applications," *J. Microw. Optoelectron. Electromagn. Appl.*, vol. 14, pp. SI-45–SI-53, 2015.

[33] M. S. Habib, O. Bang, and M. Bache, "Low-loss hollow-core anti-resonant fibers with semi-circular nested tubes," *IEEE J. Sel. Top. Quantum Electron.*, vol. 22, no. 2, 2016, Art. no. 4402106.

[34] V. Setti, L. Vincetti, and A. Argyros, "Flexible tube lattice fibers for terahertz applications," *Opt. Express*, vol. 21, no. 3, pp. 3388–3399, 2013.

[35] W. Lu, S. Lou, X. Wang, Y. Shen, and X. Sheng, "Demonstration of low-loss flexible fiber with Zeonex tube-lattice cladding for terahertz transmission," in *Proc. Opt. Fiber Commun. Conf. Exhibit.*, 2015.

[36] M. M. Nazarov *et al.*, "Eight-capillary cladding THz waveguide with low propagation losses and dispersion," *IEEE Trans. Terahertz Sc. Technol.*, vol. 8, no. 2, pp. 183–191, Mar. 2018.

[37] L. Vincetti and V. Setti, "Extra loss due to Fano resonances in inhibited coupling fibers based on a lattice of tubes," *Opt. Express*, vol. 20, no. 13, pp. 14350–14361, 2012.

[38] L. Vincetti, V. Setti, and M. Zoboli, "Terahertz tube lattice fibers with octagonal symmetry," *IEEE Photon. Technol. Lett.*, vol. 22, no. 13, pp. 972–974, Jul. 2010.

[39] A. D. Pryamikov *et al.*, "Demonstration of a waveguide regime for a silica hollow-core microstructured optical fiber with a negative curvature of the core boundary in the spectral region > 3.5 mm," *Opt. Express*, vol. 19, no. 2, pp. 1441–1448, 2011.

[40] M. Michieletto *et al.*, "Hollow-core fibers for high power pulse delivery," *Opt. Express*, vol. 24, no. 7, pp. 7103–7119, 2016.

[41] M. B. Levy and K. D. Laakmann, "Flexible waveguide for CO_2 laser surgery," *Proc. SPIE*, vol. 605, pp. 57–58, 1986.

[42] A. Hongo, K. Morosawa, K. Matsumoto, T. Shiota, Y. Matsuura, and M. Miyagi, "Transmission characteristics of germanium thin-film-coated metallic hollow waveguides for high-powered CO_2 laser light," *IEEE J. Quantum Electron.*, vol. 26, no. 9, pp. 1510–1515, 1990.

[43] G. Woyessa *et al.*, "Zeonex microstructured polymer optical fiber: Fabrication friendly fibers for high temperature and humidity insensitive Bragg grating sensing," *Opt. Mater. Express*, vol. 7, no. 1, pp. 286–295, 2017.

[44] J. Anthony, R. Leonhardt, A. Argyros, and M. C. J. Large, "Characterization of a microstructured Zeonex terahertz fiber," *J. Opt. Soc. Am. B*, vol. 28, no. 5, pp. 1013–1018, 2011.

[45] M. S. Islam *et al.*, "Broadband characterization of glass and polymer materials using THz-TDS," in *Proc. 44th Int. Conf. Infrared Millimeter Terahertz Waves*, Paris, France, 2019.

[46] M. S. Islam *et al.*, "Extremely low-loss, dispersion flattened porous-core photonic crystal fiber for terahertz regime," *Opt. Eng.*, vol. 55, no. 7, 2016, Art. no. 076117.

[47] L. Vincetti and V. Setti, "Waveguiding mechanism in tube lattice fibers," *Opt. Express*, vol. 18, no. 22, pp. 23133–23146, 2010.

[48] P. Rugeland, C. Sterner, and W. Margulis, "Visible light guidance in silica capillaries by anti-resonant reflection," *Opt. Express*, vol. 21, no. 24, pp. 29217–29222, 2013.

[49] L. Vincetti, "Numerical analysis of plastic hollow core microstructured fiber for terahertz applications," *Opt. Fiber Technol.*, vol. 15, no. 4, pp. 398–401, 2009.

[50] W. Lu and A. Argyros, "Terahertz spectroscopy and imaging with flexible tube-lattice fiber probe," *J. Lightw. Technol.*, vol. 32, no. 23, pp. 4621–4627, 2014.

[51] F. Poletti, "Nested antiresonant nodeless hollow core fiber," *Opt. Express*, vol. 22, no. 20, pp. 23807–23828, 2014.

[52] W. Belardi and J. C. Knight, "Hollow antiresonant fibers with reduced attenuation," *Opt. Lett.*, vol. 39, no. 7, pp. 1853–1856, 2014.

[53] M. S. Habib, J. E. A.-Lopez, C. Markos, A. Schülzgen, and R. A-Correa, "Single-mode, low loss hollow-core anti-resonant fiber designs," *Opt. Express*, vol. 27, no. 4, pp. 3824–3836, 2019.

[54] M. S. Islam, J. Sultana, J. Atai, M. R. Islam, and D. Abbott, "Design and characterization of a low-loss, dispersion-flattened photonic crystal fiber for terahertz wave propagation," *Optik*, vol. 145, pp. 398–406, 2017.

[55] M. S. Islam *et al.*, "Terahertz sensing in a hollow core photonic crystal fiber," *IEEE Sensors J.*, vol. 18, no. 10, pp. 4073–4080, 2018.

[56] C. M. B. Cordeiro, "Microstructured-core optical fiber for evanescent sensing applications," *Opt. Express*, vol. 14, no. 26, pp. 13056–13066, 2006.

[57] N. Chen, J. Liang, and L. Ren, "High-birefringence, low-loss porous fiber for single-mode terahertz-wave guidance," *Appl. Opt.*, vol. 52, no. 21, pp. 5297–5302, 2013.

[58] A. W. Snyder and J. Love, *Opt. Waveguide Theory*. London: Kluwer Academic, 2000.

[59] K. Nielsen *et al.*, "Bendable, low-loss Topas fibers for the terahertz frequency range," *Opt. Express*, vol. 17, no. 10, pp. 8592–8601, 2009.

[60] M. T. Sebastian, "Measurement of microwave dielectric properties and factors affecting them," in *Dielectric Materials for Wireless Communication*. Amsterdam: Elsevier, 2008, ch. 2.

[61] E. V. Fedulova *et al.*, "Studying of dielectric properties of polymers in the terahertz frequency range," in *Proc. SPIE Saratov Fall Meeting: Opt. Technol. Biophys. Med.*, Saratov, Russian Federation, Feb. 28, 2012.

[62] T. M. Levitskaya and B. K. Sternberg, "Parameters describing the material behavior in an electromagnetic field," in *Electrical Spectroscopy of Earth Materials*. Amsterdam: Elsevier, 2019, Ch. 2.

[63] H. Ademgil, "Highly sensitive octagonal photonic crystal fiber based sensor," *Optik-Int. J. Light Electron Opt.*, vol. 125, no. 20, pp. 6274–6278, 2014.

[64] T. Chen, Z. Han, J. Liu, and Z. Hong, "Terahertz gas sensing based on a simple one-dimensional photonic crystal cavity with high-quality factors," *Appl. Opt.*, vol. 53, no. 16, pp. 3454–3458, 2014.

[65] C. Liu *et al.*, "Symmetrical dual D-shape photonic crystal fibers for surface plasmon resonance sensing," *Opt. Express*, vol. 26, no. 7, pp. 9039–9049, 2018.

[66] Y. Peng *et al.*, "Temperature sensing using the bandgap-like effect in a selectively liquid-filled photonic crystal fiber," *Opt. Lett.*, vol. 38, no. 3, pp. 263–265, 2013.

[67] T. Srivastava, R. Das and R. Jha, "Highly sensitive plasmonic temperature sensor based on photonic crystal surface plasmon waveguide," *Opt. Lett.*, vol. 8, no. 2, pp. 515–521, 2013.

[68] M. Islam *et al.*, "Dual-polarized highly sensitive plasmonic sensor in the visible to near-IR spectrum," *Opt. Express*, vol. 26, no. 23, pp. 30347–30361, 2018.

[69] T. Yoshie, L. Tang, and S. Su, "Optical microcavity: Sensing down to single molecules and atoms," *Sensors*, vol. 11, no. 12, pp. 1972–1991, 2011.

[70] D. W. Vogt and R. Leonhardt, "Fano resonances in a high-Q terahertz whispering-gallery mode resonator coupled to a multi-mode waveguide," *Opt. Lett.*, vol. 42, no. 21, pp. 4359–4362, 2017.

[71] D. W. Vogt and R. Leonhardt, "Ultra-high Q terahertz whispering-gallery modes in a silicon resonator," *APL Photon.*, vol. 3, no. 5, 2018, Art. no. 051702.

[72] M. G. Zubel *et al.*, "3D-printed PMMA preform for hollow-core POF drawing," in *25th Int. Conf. Plast. Opt. Fibers* , 2016, pp. 295–300.

[73] T. H. R. Marques, B. M. Lima, J. H. Osório, L. E. D. Silva, and C. M. B. Cordeiro, "3D printed microstructured optical fibers," *Int. Microw. Optoelectronics Conf.*, 2017.

[74] J. Yang *et al.*, "3D printed low-loss THz waveguide based on Kagome photonic crystal structure," *Opt. Express*, vol. 24, pp. 22454–22460, 2016.

[75] W. Talataisong *et al.*, "Mid-IR Hollow-core microstructured fiber drawn from a 3D printed PETG preform," *Sci. Rep.*, vol. 8, 2018, Art. no. 8113.

[76] M. Islam *et al.*, "Experimental study on glass and polymers: Determining the optimal material for potential use in terahertz technology," *IEEE Access*, vol. 8, pp. 97204–97214, 2020.

[77] E. Köhler, S. Rahiminejad, and P. Enoksson, "Evaluation of 3D printed materials used to print WR10 horn antennas," *J. Phys.*, 2016, doi: 10.1088/1742-6596/757/1/012026.

[78] J. Liu, H. Liang, M. Zhang, and H. Su, "Terahertz wave transmission within metal-clad antiresonant reflecting hollow waveguides," *Appl. Opt,*, vol. 54, no. 14, pp. 4549–4555, 2015.

[79] O. Senlik, L. Tang, P. Tor-Ngern, and T. Yoshie, "Optical micorcavities clad by low-absorption electrode media," *IEEE Photon. J.*, vol. 2, no. 5, pp. 794–801, Oct. 2010.

[80] A. Benz *et al.*, "Terahertz active photonic crystals for condensed gas sensing," *Sensors*, vol. 11, no. 6, pp. 6003–6014, 2011.

[81] A. Hassani and M. Skorobogatiy, "Surface plasmon resonance-like integrated sensor at terahertz frequencies for gaseous analytes," *Opt. Express*, vol. 16, no. 25, pp. 20206–20214, 2008.

[82] B. You, J. Y. Lu, C. P. Yu, T. A. Liu, and J. L. Peng, "Terahertz refractive index sensors using dielectric pipe waveguides," *Opt. Express*, vol. 20, no. 6, pp. 5858–5866, 2012.

[83] L. Thrane, R. H. Jacobsen, P. Uhd Jepsen, and S. R. Keiding, "THz reflection spectroscopy of liquid water," *Chem. Phys. Lett.*, vol. 240, no. 4, pp. 330–333, 1995.

[84] J. T. Kindt and C. A. Schmuttenmaer, "Far-infrared dielectric properties of polar liquids probed by femtosecond terahertz pulse spectroscopy," *J. Phys. Chem.*, vol. 100, no. 24, pp. 10373–10379, 1996.

[85] J. Xu, "Absorption spectra of liquid water and aqueous buffers between 0.3 and 3.72 THz," *J. Chem. Phys.*, vol. 124, 2006, Art. no. 036101.

[86] N. Y. Tan *et al.*, "Probing hydrogen-bonding in binary liquid mixtures with terahertz time-domain spectroscopy: A comparison of Debye and absorption analysis," *Phys. Chem. Chem. Phys.*, vol. 18, no. 8, pp. 5999–6008, 2015.

[87] A. L. S. Cruz, A. C. C. Migliano, and M. A. R. Franco, "Refractive index sensor based on terahertz multimode interference fiber device," in *Proc. SPIE 5th Eur. Workshop Opt. Fibre Sensor*, 2013.

[88] J. Li, K. Nallappan, H. Guerboukha, and M. Skorobogatiy, "3D printed hollow core terahertz Bragg waveguides with defect layers for surface sensing applications," *Opt. Express*, vol. 25, no. 4, pp. 4126–4144, 2017.

[89] Y. Cao, K. Nallappan, H. Guerboukha, T. Gervais, and M. Skorobogatiy, "Additive manufacturing of resonant fluidic sensors based on photonic bandgap waveguides for terahertz applications," *Opt. Express*, vol. 27, no. 20, pp. 27663–27681, 2019.

[90] A. I. McIntosh, B. Yang, S. M. Goldup, M. Watkinson, and R. S. Donnan, "Terahertz spectroscopy: A powerful new tool for the chemical sciences," *Chem. Soc. Rev.*, vol. 41, no. 6, pp. 2072–2082, 2012.

[91] MenloSystems, *Terahertz Antennas Compon.*, 2017. Available: http://www.menlosystems.com/

[92] W. Talataisong, R. Ismaeel, M. Beresna, and G. Brambilla, "Suspended-core microstructured polymer optical fibers and potential applications in sensing," *Sensors*, vol. 19, no. 6, 2019, Art. no. 3449.

[93] M. Taherkhani, R. A. Sadeghzadeh, J. Taiber, J. Ornik, and M. Koch, "The effect of humidity and temperature on dielectric fibre-bound THz transmission," *J. Infrared Milli. Terahertz Waves*, vol. 40, pp. 1092–1102, 2019.

[94] S. Yang, X. Sheng, G. Zhao, Y. Wang, and Y. Yu, "Novel pentagram THz hollow core anti-resonant fiber using a 3D printer," *J. Infrared Millimeter Terahertz Waves*, vol. 40, no. 7, pp. 720–730, 2019.

Jakeya Sultana received the B.Sc. in Eng. degree in electronics & telecommunication engineering from the Rajshahi University of Engineering and Technology and the M.Sc. in Eng. degree in electrical & electronic engineering from the Islamic University of Technology, Bangladesh, in 2014 and 2017, respectively. She is working toward the Ph.D. degree at the School of Electrical and Electronic Engineering, The University of Adelaide, Australia.

Her research interests include antiresonant fibers for terahertz applications and supercontinuum generation.

Sultana is an active reviewer for *Journal of Lightwave Technology*, IEEE PHOTONIC TECHNOLOGY LETTERS, *Optik*, and *Optics Communications*.
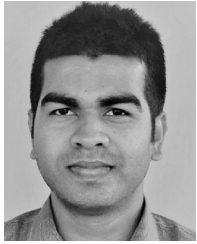
Md. Saiful Islam (Member, IEEE) is working toward the Ph.D. degree at the School of Electrical and Electronic Engineering, The University of Adelaide, Australia.

He has authored/co-authored 43 peer-reviewed articles. His research interests include optical fiber communication, PCF-based terahertz waveguides, terahertz sensors, surface plasmon resonance biosensors, topological insulators, and metamaterials for sensing applications.

Islam is a member of IEEE, IEEE Young Professionals, Optical Society of America (OSA), and Institute for Photonics & Advanced Sensing (IPAS). He is a reviewer for *Scientific Reports*, *Photonics Research*, IEEE JOURNAL OF LIGHTWAVE TECHNOLOGY, IEEE PHOTONICS JOURNAL, IEEE SENSORS JOURNAL, IEEE PHOTONICS TECHNOLOGY LETTERS, *Optics Express, Applied Optics*, *Optical Materials Express*, *Optical Fiber Technology*, etc. He has been as recognized as a top peer reviewer in physics and cross-fields in 2019 by Publons and Web of science.

Cristiano M. B. Cordeiro received the Ph.D. degree from the University of Campinas (UNICAMP), Brazil.

He held a Postdoctoral position with the University of Bath, England. He is currently an Assistant Professor with the Institute of Physics, UNICAMP and Head of the Specialty Optical Fiber Laboratory. He is the author of 70 journal publications, 50 communications in international conferences, a book chapter, and eight patents. His research interests include the development and application of silica photonic crystal fibers, microstructured polymer optical fibers, and micro/nanofibers, and exploring new fiber functionalities and the use of new technologies in the optical fiber area.

Dr.Cordeiro chaired the first Workshop on Specialty Optical Fibers (WSOF), which is now in its sixth cycle.

Md. Selim Habib (Senior Member, IEEE) received the B.Sc. and M.Sc. degrees in electrical and electronic engineering from the Rajshahi University of Engineering & Technology, Rajshahi, Bangladesh, in 2008 and 2012, respectively. He received the Ph.D. degree in photonics engineering from the Technical University of Denmark (DTU), in 2017.

He was a Postdoctoral Researcher with Fibers Sensors and Supercontinuum Group, Department of Photonics Engineering, DTU. He was a Postdoctoral Research Associate with CREOL, The College of Optics and Photonics, University of Central Florida, USA, from September, 2017 to August, 2019. Currently, he is an Assistant Professor of Electrical and Computer Engineering with Florida Polytechnic University, USA. His research interests include design, fabrication, and characterization of low-loss hollow-core fiber in the near-IR to mid-IR, light gas nonlinear interaction in hollow-core fibers, supercontinuum generation, and multimode nonlinear optics.

Dr. Habib is a Senior Member of Institute of Electrical and Electronics Engineers (IEEE), Optical Society of America (OSA) Early Careers Member, and Executive officer of OSA Fiber modeling and Fabrication group. He is an Associate Editor of IEEE ACCESS and Topic Editor of *Fibers*. He received the University Gold Medal Award from the Rajshahi University of Engineering & Technology, in 2014.

Alex Dinovitser (Graduate Student Member, IEEE) received the B.Eng. (Hons.) degree in electrical and computer systems engineering from Monash University, Melbourne, VIC, Australia, in 1991. He received the B.Sc. (Hons.) degree in physics, in 2005. He received the Ph.D. degree in physics from the University of Adelaide, Adelaide, SA, Australia, in 2012.

He has worked within the electronics manufacturing industry, designing computer interface, and signal acquisition systems. His career then spanned from optical metrology to computer simulation modeling. In 2008, he built the first spectroscopic Lidar in Australia for the differential absorption detection of atmospheric trace gases. Since 2013, he has been a Postdoctoral Fellow with The National T-ray Facility, University of Adelaide.

Dr. Dinovitser is also a member of the Optical Society of America (OSA) and Engineer's Australia.

Mayank Kaushik was born in Gujarat, India, in 1983. He received the bachelor's (with Hons.) degree in electronic and telecommunication engineering from the NRI Institute of Information Science and Technology, Bhopal, India, in 2005, the master's degree in electronic and telecommunication engineering from the University of Adelaide, Adelaide, SA, Australia, in December 2007, where he successfully designed, developed and implemented a new technique for radio frequency stabilization with significantly reduced phase noise, under the supervision of Christopher Coleman, and the Ph.D. degree in electrical & electronic engineering from The University of Adelaide, Adelaide, SA, Australia, under the supervision of Brian W.-H. Ng, Bernd M. Fischer, and Derek Abbott, in 2013.

During the bachelor's degree, he was a trainee with the Microwave Remote Sensing Area (MRSA) and Microwave Sensors Data Acquisition and Processor Division (MSDAPD), Space Applications Centre, Ahmedabad, Indian Space Research Organisation, under the supervision of Nilesh M. Desai, in the area of digital pulse compression and successfully designed a synthetic aperture radar range compression chip. Immediately after that, he was appointed as a Research Assistant at the University of South Australia (and later at the University of Adelaide) to work on various audio signal processing related projects for the then Defence Science and Technology Organisation (DSTO), now called DST. In 2012, he joined the DST, Edinburgh, Australia, as a Radar Research Scientist.

Dr. Kaushik was the recipient of two IEEE South Australia Section Travel Scholarship Awards and the Walter & Dorothy Duncan Trust Travel Award during the Ph.D.
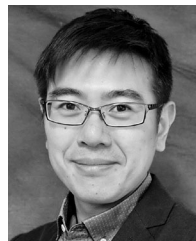
Brian W.-H. Ng (Member, IEEE) received the Ph.D degree in electrical & electronic engineering from The University of Adelaide, Adelaide, SA, Australia.

He is currently a Senior Lecturer with the School of Electrical and Electronic Engineering, University of Adelaide, Adelaide, SA, Australia. His research interests include radar signal processing, wavelets, and terahertz (T-ray) signal processing.

Dr. Ng received the University of Adelaide Medal for the Top Graduate in Electrical and Electronic Engineering. He is currently an active member within the South Australian Chapter of the IEEE.

Heike Ebendorff-Heidepriem received the Ph.D. degree in chemistry from the University of Jena, Germany, in 1994.

During 2001–2004, she was with the Optoelectronics Research Centre, University of Southampton, U.K. Since 2005, she has been with the University of Adelaide, Australia. Currently, she is the Deputy Director of the Institute for Photonics and Advanced Sensing, Adelaide, Australia. Her research interests include the development of novel optical glasses, specialty optical fibers, surface functionalization, and sensing approaches.

Dr. Ebendorff-Heidepriem received the Weyl International Glass Science Award and the prestigious Marie Curie Individual Fellowship in 2001.

Derek Abbott (Fellow, IEEE) was born in South Kensington, London, U.K. He received the B.Sc. (Hons.) degree in physics from Loughborough University, Leicestershire, U.K., in 1982, and the Ph.D. degree in electrical and electronic engineering from the University of Adelaide, Adelaide, SA, Australia, in 1995.

His research interests include multidisciplinary physics and electronic engineering applied to complex systems. His research programs span a number of areas of stochastics, game theory, photonics, energy policy, biomedical engineering, and computational neuroscience.

Dr. Abbott is a Fellow of the Institute of Physics, U.K., and an Honorary Fellow of Engineers Australia. He has won a number of awards, including the South Australian Tall Poppy Award for Science (2004), the Premier's SA Great Award in Science and Technology for outstanding contributions to South Australia (2004), an Australian Research Council Future Fellowship (2012), the David Dewhurst Medal (2015), and the Barry Inglis Medal (2018), and the M.A. Sargent Medal (2019). He has served as an Editor and/or Guest Editor for a number of journals, including the IEEE JOURNAL OF SOLID STATE CIRCUITS, *Journal of Optics B*, *Microelectronics Journal*, *Chaos*, *Smart Structures and Materials*, *Fluctuation and Noise Letters*, PROCEEDINGS OF THE IEEE, and IEEE PHOTONICS JOURNAL. He has served on the Editorial Board of PROCEEDINGS OF THE IEEE (2009–2014), the Editorial Board of IEEE ACCESS (2015–Present), and he currently serves (2019–Present) on the IEEE Publications Publication Services and Products Board (PSPB).